FOUNDATIONS
ADVANCES

ISSN: 2053-2733
journals.iucr.org/a

The characteristic radiation of copper $K\alpha_{1,2,3,4}$

Hamish A. Melia, Christopher T. Chantler, Lucas F. Smale and Alexis J. Illig

Acta Cryst. (2019). A**75**, 527–540

Acta Cryst A FOUNDATIONS ADVANCES

ISSN 2053-2733

Received 28 November 2018
Accepted 23 January 2019

Edited by L. D. Marks, Northwestern University, USA

Keywords: X-ray characteristic radiation; Cu $K\alpha$; profile analysis; X-ray spectroscopy; shake probability.

The characteristic radiation of copper $K\alpha_{1,2,3,4}$

Hamish A. Melia, Christopher T. Chantler,* Lucas F. Smale and Alexis J. Illig

School of Physics, University of Melbourne, Australia. *Correspondence e-mail: chantler@unimelb.edu.au

A characterization of the Cu $K\alpha_{1,2}$ spectrum is presented, including the $2p$ satellite line, $K\alpha_{3,4}$, the details of which are robust enough to be transferable to other experiments. This is a step in the renewed attempts to resolve inconsistencies in characteristic X-ray spectra between theory, experiment and alternative experimental geometries. The spectrum was measured using a rotating anode, monolithic Si channel-cut double-crystal monochromator and backgammon detector. Three alternative approaches fitted five Voigt profiles to the data: a residual analysis approach; a peak-by-peak fit; and a simultaneous constrained method. The robustness of the fit is displayed across three spectra obtained with different instrumental broadening. Spectra were not well fitted by transfer of any of three prior characterizations from the literature. Integrated intensities, line widths and centroids are compared with previous empirical fits. The novel experimental setup provides insight into the portability of spectral characterizations of X-ray spectra. From the parameterization, an estimated $3d$ shake probability of 18% and a $2p$ shake probability of 0.5% are reported.

1. Introduction

The spectrum given by the characteristic radiation of atoms is used in a number of fields of science including chemistry (Kawai *et al.*, 1994), astrophysics (Sulentic *et al.*, 1998), plasma physics (Hansen *et al.*, 2005), nanopowders (Armelao *et al.*, 2008) and medicine (Uo *et al.*, 2015). More specifically the $K\alpha$ line is used as a calibration standard in many X-ray experiments. For example, theoretical determination of features in X-ray spectra requires calibration accurate down to the one part per million (p.p.m.) level in high-accuracy tests of quantum electrodynamics (Gillaspy *et al.*, 2010; Chantler, Kinnane *et al.*, 2012; Smale *et al.*, 2015). The characteristic radiation and photoemission lines of copper provide a benchmark for both experimental and theoretical X-ray calibration in the transition metals. The $K\alpha$ line, caused by the $2p \rightarrow 1s$ transition, is a doublet due to the fine structure splitting of the $2p$ subshell. The magnitude of the splitting is determined by relativistic effects and therefore is dependent on the atomic number, Z. The $K\beta$ line is a result of the $3p \rightarrow 1s$ transition.

High-accuracy determination of the structure and energies of X-ray emission profiles is required for energy calibration in a wide range of scientific experiments. In particular, X-ray line shapes and energies are important in high-accuracy characterization of crystallographic measurements at synchrotron and standard laboratories worldwide. The *International Tables for Crystallography* Volume C (2019) provides detailed treatises on the experimental and theoretical characterization of X-ray standards, X-ray profiles and absorption edges. The ability to tie the X-ray energy scale to the definition of the metre, through the lattice parameter of standard reference

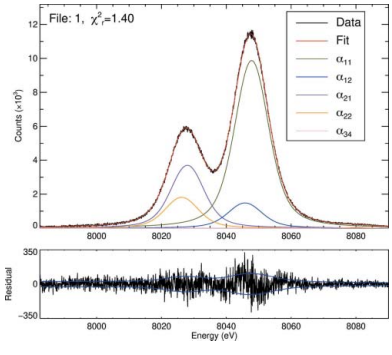

Table 1
Characterizations of the Cu $K\alpha_{1,2}$ and $K\alpha_{3,4}$, the $K\alpha''$ $2p$ satellite, with peak centroid and FWHM estimates for peak energies $K\alpha_1^0$ and $K\alpha_2^0$.

The satellite FWHM components vary significantly across these prior characterizations.

Component	Energy (eV)	FWHM (eV)	Area (%)	ΔE
Mendenhall *et al.* (2017)†	$I(K\alpha_2)/I(K\alpha_1)$ = 0.520 (1)			*cf.* Mendenhall *et al.* (2017)
$K\alpha_{11}$	8047.8254 (3)	2.275 (1)	58.28 (3)	
$K\alpha_{12}$	8045.2956 (47)	2.915 (9)	7.07 (3)	
$K\alpha_1^0$	8047.817 (8)(20)(60)‡			
$K\alpha_{21}$	8028.0503 (27)	2.529 (5)	22.81 (13)	
$K\alpha_{22}$	8026.5386 (92)	3.274 (8)	11.24 (13)	
$K\alpha_2^0$	8027.94 (2)(6)‡			
$K\alpha''$	8081.7	12.6	0.57 (2); 0.61(2)§	
Hölzer *et al.* (1997)¶	$I(K\alpha_2)/I(K\alpha_1)$ = 0.517 (20)			
$K\alpha_{11}$	8047.837 (2)	2.285 (3)	57.9 (1)	0.012 (2)
$K\alpha_{12}$	8045.367 (22)	3.358 (27)	8.0 (1)	0.071 (22)
$K\alpha_1^0$	8047.83 (1)	2.35		
$K\alpha_{21}$	8027.993 (5)	2.666 (7)	23.6 (1)	0.057 (5)
$K\alpha_{22}$	8026.504 (14)	3.571 (23)	10.5 (1)	0.035 (14)
$K\alpha_2^0$	8027.85 (1)	3.41		
Fritsch *et al.* (1998)¶ $K\alpha''$	8081.6	5.90	–	0.1
Illig *et al.* (2013)††	$I(K\alpha_2)/I(K\alpha_1)$ = 0.498 (6)			
$K\alpha_{11}$	8047.947 (54)	2.484 (60)	64.6 (3)	0.122 (54)
$K\alpha_{12}$	8044.142 (481)	0.755 (101)	1.4 (1)	1.15 (48)
$K\alpha_{21}$	8028.272 (170)	2.489 (145)	21.7 (1)	0.22 (17)
$K\alpha_{22}$	8026.644 (311)	3.089 (298)	11.2 (1)	0.105 (311)
$K\alpha''$	8076.623 (25)	3.844 (3)	0.215 (1)	5.000 (25)
Deutsch *et al.* (1995)‡‡	$I(K\alpha_2)/I(K\alpha_1)$ = 0.534 (9)			
$K\alpha_{11}$	8047.837 (6)	2.298 (7)	57.5 (4)	0.012 (6)
$K\alpha_{12}$	8045.293 (52)	3.068 (64)	7.6 (2)	0.003 (52)
$K\alpha_1^0$		2.30 (2)		
$K\alpha_{21}$	8028.022 (13)	2.710 (17)	24.4 (3)	0.028 (13)
$K\alpha_{22}$	8026.562 (40)	3.560 (57)	10.4 (3)	0.023 (40)
$K\alpha_2^0$		3.34 (6)		

† Double-crystal monochromator in single-crystal mode, relative measurement. ‡ Quoted uncertainty but not recommended in paper due to systematics of magnitude 0.02, 0.06 eV shown in the paper. § First estimate based on tabulated components; second based on correlated sum estimate. ¶ Single-crystal results with deconvolved spectra. †† Double-crystal measurement, deconvolved. ‡‡ Double-crystal results, relative measurement.

materials, has made the precision in X-ray energy measurements, particularly Cu $K\alpha$, on the order of 1 p.p.m.

The spectrum is dominated by the diagram lines: $K\alpha_1$, $[1s]^{-1} \rightarrow [2p_{3/2}]^{-1}$, and $K\alpha_2$, $[1s]^{-1} \rightarrow [2p_{1/2}]^{-1}$. Satellite lines are caused by the presence of an outer-shell hole when an electron decays from the $2p$ to the $1s$ shell (Parratt, 1936*b*). The extra hole causes a change in electron configuration and hence a change in energy of the emitted photon. These outer-shell holes are thought to be created during the bombardment of the target metal through *shake processes*. The term 'shake processes' refers to when the photoelectron interacts with an outer-shell electron of the target atom, either freeing it from the atom (shake off), or exciting it to a higher state (shake up) (Pham *et al.*, 2016). These processes give an explanation for the presence of outer-shell holes that create asymmetries in the spectrum. By measuring the contribution of the satellite lines to the spectra we can estimate the probability of this atomic process, often referred to as the *shake probability*.

These multiple electron transitions force us to think beyond an independent electron model, where electrons are thought to only interact with the nucleus, and to consider a model that can include electron–electron interactions (Diamant *et al.*, 2009). The change in spectra caused by satellite lines, through multi-electron transitions, can be used to study electronic correlations within the atom. In the adiabatic region, near the energy threshold for multi-electron transitions, the ejected electron has relatively low kinetic energy, so that the overlap with the atom is larger and correlation is more prominent than in the high-energy isothermal regime. In the adiabatic regime we can consider the excitation and decay to be one process, while in the isothermal regime we can consider these as two sequential processes (Crasemann, 1987).

Although studied extensively throughout the last century, there remain inconsistencies between theory and experiment with regard to the shape of the Cu $K\alpha$ spectrum. Current theories are still not able to fully account for asymmetries present in the spectra. An asymmetrical peak indicates that structure more complex than a symmetric bound–bound transition must be present. Asymmetries have been explained in a number of different ways: as Kondo-like many-electron interactions (Doniach & Sunjic, 1970); as two-electron transitions such as shake processes (Parratt, 1959); as interactions in the final state between the $1s$ hole and higher-shell unpaired electrons (Sorum, 1987); and as an electrostatic exchange between $2p$ and $3d$ electron shells (Pham *et al.*, 2016). Others have stated that assigning asymmetries to this exchange is *only partially satisfactory* (Salem & Wimmer, 1970). Deutsch *et al.* (1995) have predicted that the only appreciable contribution to the Cu $K\alpha$ spectrum are the diagram lines and the $3d$ hole spectator lines. However, recent work indicates very significant contributions from other satellites, both theoretically and experimentally (Fritsch *et al.*, 1998; Pham *et al.*, 2016).

2. The problem of X-ray characteristic radiation

Table 1 indicates the major and most recent characterizations of the Cu $K\alpha$ spectrum from experimental data. Table 4 of Illig *et al.* (2013) reports, from their parameterization, a peak height ratio, $P(K\alpha_2)/P(K\alpha_1) = 0.514\ (3)$; given the widths this is identical to an integrated intensity ratio of $I(K\alpha_2)/I(K\alpha_1) = [I(K\alpha_{21}) + I(K\alpha_{22})]/[I(K\alpha_{11}) + I(K\alpha_{12})] = 0.498\ (6)$, where $I(K\alpha_{ij})$ refers to the fitted integrated intensity, or area, of that particular component, given as a percentage to the total spectrum.

Clearly, component energies, full width at half-maximum (FWHM) and relative integrated intensities vary significantly over the four parameterizations. In particular, Hölzer *et al.* (1997) and Mendenhall *et al.* (2017) provide independent absolute characterizations of the Cu $K\alpha_{1,2}$ spectrum using sums of Lorentzians. Each demonstrates an excellent fit to the experimental data.

However, the parameters reported vary significantly (Table 2). Discrepancies as large as 16% are evident in FWHM component parameters for the pure Lorentzians, with discrepancies of 5 and 7 standard errors on the dominant component centroids and peak shifts by numerous standard errors. The $K\alpha_{3,4}$ satellite structure varies quite dramatically in width and structure between characterizations. Further, the sum of components in terms of peak energies and peak shapes varies significantly (Table 1, Fig. 1).

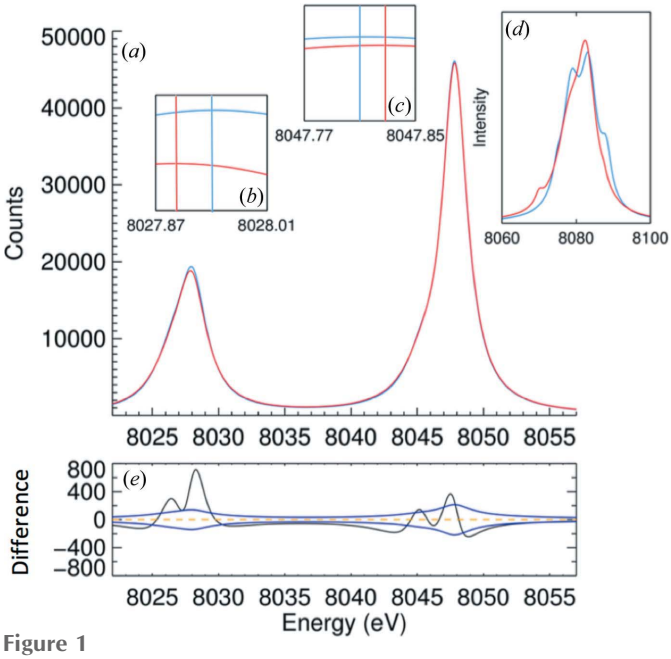

Figure 1
(*a*) The two best characterizations of Cu $K\alpha_{1,2}$: red line, Hölzer *et al.* (1997); blue line, Mendenhall *et al.* (2017). Tables 1 and 2 present the parameters for each component. (*b*) The two parameterizations around the $K\alpha_2$ peak. The vertical lines indicate the maximum of each profile characterization. (*c*) The two parameterizations around the $K\alpha_1$ peak. The vertical lines indicate the maximum of each profile characterization. (*d*) shows the parameterization of the $K\alpha_{3,4}$ complex given by Mendenhall *et al.* (2017) (blue) and Fritsch *et al.* (1998) (red). (*e*) The difference between the two characterizations (black line) is structured and larger than the associated standard error [dark blue line, $(N)^{1/2}$] indicating locations of disagreement between the two parameterizations.

Table 2
Difference in parameters of Cu $K\alpha_{1,2}$ spectra between Hölzer *et al.* (1997) and Mendenhall *et al.* (2017).

The lower panel shows the difference as a fraction of the sum of 1σ (standard errror) uncertainties.

Component	Energy (eV)	FWHM (eV)	Area (%)
$K\alpha_{11}$	−0.012	−0.010	0.402
$K\alpha_{12}$	−0.072	−0.443	−0.932
$K\alpha_{21}$	0.057	−0.137	−0.786
$K\alpha_{22}$	0.035	−0.297	0.743
Shifts with respect to parameter standard errors			
$K\alpha_{11}$	-5.095σ	-2.500σ	2.997σ
$K\alpha_{12}$	-2.688σ	-12.306σ	-6.957σ
$K\alpha_{21}$	7.419σ	-11.417σ	-3.464σ
$K\alpha_{22}$	1.494σ	-9.581σ	3.272σ

While these two characterizations of Lorentzian fits look sound, and are certainly at the cutting edge for experimental work, in the case of Mendenhall *et al.* (2017) no χ^2_r or goodness of fit is reported in the paper. Furthermore, when the Mendenhall *et al.* fit is presented with the associated residuals, as in the supplementary material, the data do not obey Poissonian $(N)^{1/2}$ statistics from a coherent spectrum. Bin statistics and the pooling of many data sets have also meant that the data cannot be naturally refitted. Pooling the data in this way may create problems with portability and broadening. Other recent important contributions have been made by Härtwig *et al.* (1993), Deutsch *et al.* (1995), Fritsch *et al.* (1998), Illig *et al.* (2013) and Ito *et al.* (2016).

The degeneracy of the $2p_{3/2}$ level is twice that of the $2p_{1/2}$ making the probability of a $K\alpha_1$ transition double that of the $K\alpha_2$ transition, *i.e.* the integrated intensity ratio $I(K\alpha_2)$:$I(K\alpha_1)$ of the peaks should be 1:2. Experimentally this ratio increases with atomic number (Salem & Wimmer, 1970; Hölzer *et al.*, 1997; McCrary *et al.*, 1971). How and why this ratio increases with Z is of particular importance when explaining inner-shell processes across the 3*d* transition metals (Sorum, 1987). Initial attempts to match theory and experiment, using single particle states in a potential given by relativistic Hartree–Slater theory, gave discrepancies with regard to atomic number trends, especially $I(K\alpha)/I(K\beta)$ (Scofield, 1969; Lu *et al.*, 1971). This led to more sophisticated relativistic Hartree–Fock calculations, that include exchange effects of the nonzero overlap of wavefunctions from different subshells, that were able to match the experimental trends with Z (Scofield, 1974). Multi-configuration Dirac–Fock calculations of copper have more recently been successful in explaining the observed intensity ratios through the inclusion of exchange effects, fine structure contributions and the modelling of spectator holes in all of the 3*p*, 3*d* and 4*s* shells (Chantler *et al.*, 2010).

The integrated intensity ratio $I(K\alpha_2)/I(K\alpha_1)$ of the peaks for Cu has been reported widely in the literature, both through theory and experiment. However, accurate values are still unclear. Scofield *et al.* computed the ratio theoretically to be 0.5124 (Scofield, 1969) and 0.5133 (Scofield, 1974). The best Cu X-ray emission experiments measure the ratio at 0.517 (20) (Hölzer *et al.*, 1997) and 0.520 (2) (Mendenhall *et al.*, 2017).

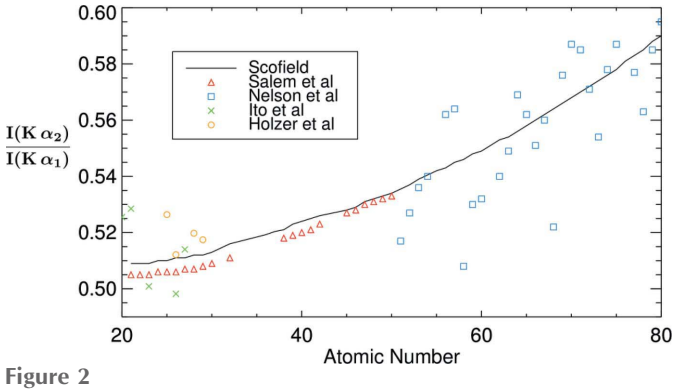

Figure 2
The $I(K\alpha_2)/I(K\alpha_1)$ ratio as a function of atomic number. The points are experimental from references (Salem & Wimmer, 1970; Nelson & Saunders, 1969; Ito *et al.*, 2016; Hölzer *et al.*, 1997) The line shows the theoretical predictions of Scofield (1974). The exact ratio for Cu is not yet known; however we expect it to be greater than 0.51, less than 0.52, and probably 0.510 (5).

The ratio has been reported to be as low as 0.478 (Berger, 1986). However, since then it has consistently been found experimentally to be above 0.51 (Sorum, 1987; Härtwig *et al.*, 1993; Deutsch *et al.*, 1995; Hölzer *et al.*, 1997; Mendenhall *et al.*, 2017). Fig. 2 shows the $I(K\alpha_2)/I(K\alpha_1)$ ratio as a function of atomic number for $20 \leq Z \leq 80$. Large discrepancies between literature values, both theoretical and experimental, remain.

This article is part of a renewed attempt to resolve inconsistencies between theory and experiment concerning the shape of the spectrum, highlighted by the variation between the best current analyses and by the need for characterizations for conventional X-ray sources or for fluorescent sources at synchrotrons. Some may naively think that because the best theoretical and the best experimental work have been done on Cu $K\alpha$, compared with any other element or bound transition except hydrogen and helium, that this is a closed inquiry. However, this is not the case as we detail herein. More work remains to be done on the understanding of transition metal K spectra, absolutely including that of copper. For this work, four critical questions are:

(i) Do the excellent prior experimental investigations of copper $K\alpha$ permit a transferable standard, and if so under what conditions?

(ii) Can we obtain a new characterization with standard sources (the rotating-anode or laboratory-source geometries), together with novel backgammon detection, and is it consistent with these prior characterizations?

(iii) What significance and application might the new characterization from the novel but more standard experimental setup obtain?

(iv) How might new or older characterizations need to be adapted for standard laboratory and synchrotron measurements and calibrations?

These questions are the focus of this article.

3. Experiment

The characteristic radiation used was generated by a rotating-anode source and measured using a backgammon-type multiwire gas proportional counter (MWPC). The beam was diffracted using a monolithic Si(111) channel-cut crystal and projected onto the detector face. Three data sets of the Cu $K\alpha$ spectrum were measured along with a background image. The three data sets will be described as File 1, File 2 and File 3 throughout the text. Full details of the experiment, detector and initial processing steps (Melia *et al.*, 2019) are summarized in Appendix *A*.

4. Profile

The spectrum of transition metals has typically been represented by the sum of peaks. The spectrum with no instrumental broadening is approximated by the sum of four or five Lorentzian functions (Berger, 1986) and this has been implemented by previous fits to experimental data for the Cu $K\alpha$ spectra. This distribution can be obtained through a deconvolution of the measured spectrum and then modelled (Hölzer *et al.*, 1997; Deutsch *et al.*, 1995). Homogeneous sources of broadening, such as lifetime or pressure are Lorentzian broadening functions. Other sources of broadening, such as Doppler or thermal broadening, are normally distributed and can be represented with a (common) Gaussian function. A Voigt profile – the convolution of a Lorentzian and a Gaussian – has been used in this work, as this type of profile captures both natural homogeneous broadening and normal inhomogeneous broadening. Voigt profiles have been shown to successfully model the spectrum of Cu $K\alpha$ and can easily be separated into Gaussian and Lorentzian contributions (Illig *et al.*, 2013). To match the modelling of real laboratory spectra with those of standards laboratories with minimal or no instrumental broadening, ideally one can simply fit the spectra and, following the fit, set a (common) Gaussian instrumental broadening width to zero to recover or compare with the high-resolution ansatz.

Early work suggested that the two peaks $K\alpha_{12}$ and $K\alpha_{22}$ are the result of higher-shell vacancies (Sauder *et al.*, 1977). Specifically, it is often presumed in recent literature that the spectrum is made up of five main contributions. The diagram lines ($K\alpha_{11}$, $K\alpha_{21}$) due to transitions: $[1s]^{-1} \rightarrow [2p_{3/2}]^{-1}$ and $[1s]^{-1} \rightarrow [2p_{1/2}]^{-1}$; two $3d$ satellite contributions: the $K\alpha_{12}$, $[1s3d]^{-1} \rightarrow [2p_{3/2}3d]^{-1}$, and the $K\alpha_{22}$ satellite line, $[1s3d]^{-1} \rightarrow [2p_{1/2}3d]^{-1}$ transition; and lastly a much smaller $2p$ satellite. The $2p$ satellite is labelled as $K\alpha''$ (Parratt, 1936*a*) or $K\alpha_{3,4}$ and is dominated by the transitions $[1s2p]^{-1} \rightarrow [2p]^{-2}$. Diamant *et al.* (2006) show theoretically that the $K\alpha''$ spectral feature may be composed of seven separate overlapping components centred at 8080 eV with a large total FWHM of approximately 5.9 or 6.25 eV; conversely, Mendenhall *et al.* (2017) measure a width of 12.6 eV. The two results are not consistent.

The function used in this work to fit the data was the addition of five Voigt profiles, one for each transition, plus the background component. Full details and definitions are shown in Appendix *B*.

The spectrum was projected onto a 40 × 40 mm beryllium window and photon–gas interactions measured in two dimensions. Processing of raw data is detailed in the work of

Melia *et al.* (2019). The average nonlinearity of the detector used was of the order of 1 µm, making uncertainty in the energy scale on the order of 5 p.p.m. The relatively large size of pixels in segmented detectors leads to potential aliasing issues.

The path length of the X-ray beam from the source slit to detector face was approximately 80 cm. Air absorption of X-rays will vary energy along this length and affect intensity; however, we expect this uncertainty to be small and the overall uncertainty in intensity to be dominated by counting statistics. Accounting for air absorption, detector efficiency or other systematics in the fit without adding free parameters may be possible in some cases; however, with the current experimental geometry and detector it is not thought to be significant. Additional fitting parameters, in our case, would likely skew the χ^2_r of our results without providing significant improvements.

5. Analysis: a residual analysis approach

The residual analysis (RA) approach used for fitting successive Voigts was based on work previously developed by our group (Illig *et al.*, 2013), the logic of which has been used to find the position of satellite lines in the past (Sorum & Bremer, 1982). The spectrum was fitted initially with two Voigts. A residual to the fit was calculated and modelled using a sum of a number of Gaussians, locating the largest features in the residual. Another Voigt was then added, using the position of the largest amplitude component in the RA as the initial guess for the additional peak. Voigts were added in this way until a total of five were present. The largest peaks in the residual show where the model and data disagree most, possibly indicating that a physical process, a transition present in the spectrum, is not being well accounted for at that point. Further discussion of this is given in Appendix *C*, including a discussion of the limitations thereof.

6. Analysis: peak-by-peak fit approach

An RA will not always work. The next Voigt should be added to where the fit and data disagree most with a reasonable width. However, the RA will not always find this position correctly, usually due to the complexity of the residual and correlation of the spectral components. For this reason the data were fitted with initial estimates from Hölzer *et al.* (1997). This fit was constrained to avoid zero amplitude components. When adding to the spectra peak by peak the new fit is dependent on the last, so when adding the third peak the Lorentzian broadening is already well accounted for by the first two peaks and so the added peak has a low Lorentzian width. However, the satellite lines should be *broader* than the diagram lines (Table 3). To correct for this problem the FWHMs of the $K\alpha_{11}$ and $K\alpha_{12}$ peaks have been constrained to the $K\alpha_{21}$ and $K\alpha_{22}$ FWHMs.

Relatively similar results were obtained for all three data sets, with good fits and reasonable widths. This procedure is more robust than a RA approach. Table 3 shows parameters obtained by the peak-by-peak approach for the File 1 spectrum. A comparison of Figs. 3, 4 and 5 shows the variation between data sets and the remaining significant discrepancies compared with the literature.

Table 3
Peak-by-peak fit for the File 1 data set with good χ^2_r.

The peak-by-peak fit was much more robust compared with the RA approach. However, like the RA fit, satellite line widths are lower than expected (see text).

Channel size (eV)	Gaussian FWHM (eV)	$I(K\alpha_2)/I(K\alpha_1)$	χ^2_r
0.059	3.892 (12)	0.492 (11)	1.398

Component	Energy (eV)	Lorentzian FWHM (eV)	Area (%)
$K\alpha_{11}$	8047.837 (5)	5.665 (14)	58.350 (57)
$K\alpha_{12}$	8045.778 (296)	As above	8.753 (9)
$K\alpha_{21}$	8027.993 (90)	5.199 (36)	21.875 (80)
$K\alpha_{22}$	8026.239 (282)	As above	10.719 (11)
$K\alpha''$	8080.141 (193)	0.244 (375)	0.303 (12)

7. Analysis: transfer of a standard from literature characterizations

Hölzer *et al.* (1997), Illig *et al.* (2013) and Mendenhall *et al.* (2017) have each reported fits to the experimental profiles of Cu $K\alpha$. Each of these prior characterizations should ideally be indistinguishable, so that any one of these three can be used as the transferable standard for the energy calibration or spectral calibration of Cu $K\alpha$ in its myriad applications – so long as

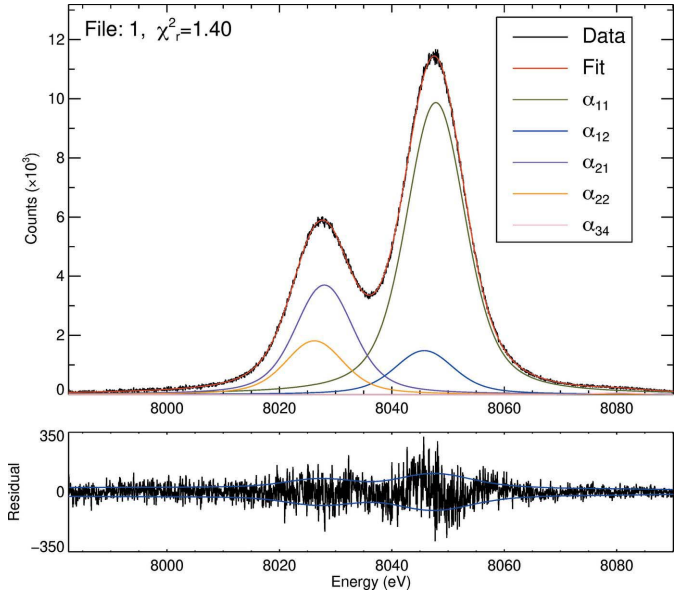

Figure 3
Peak-by-peak fit to the File 1 data set. The overall structure of the spectrum is similar to that of Hölzer *et al.* (1997) by design, compared with a residual analysis approach (Appendix *C*; Section 5). The residual is noisy but with some structure as well known in the literature; the blue line is the ±1 standard error uncertainty map to indicate the significance of particular discrepancies.

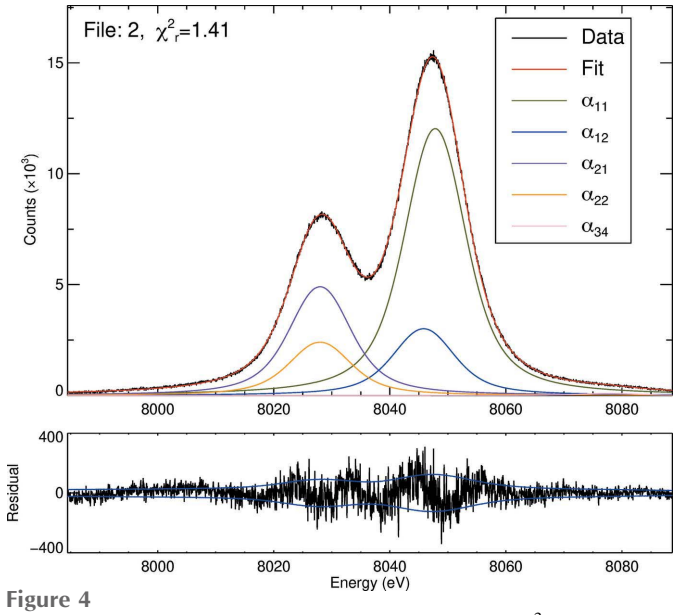

Figure 4
Plots of the peak-by-peak fit to the File 2 data set. The χ^2_r remains good.

allowance can be made for the instrument or point spread function (PSF) or the change in PSF from one characterization to another. As seen in Section 1 and below, the characterizations are qualitatively different and distinguishable using these data sets.

To attempt to transfer a standard characterization assumes explicitly that each is an ideal transfer standard except for the natural change in PSF and instrument function from one experimental geometry to another. Hence here we recreate the profiles they found, normalized and fitted to our data. Common Voigt broadening was required to account for the instrumental component of our data not present, or already deconvoluted, in the reference characterizations. Centroid positions of $K\alpha_{11}$ and $K\alpha_{21}$ were left free to define the energy scale. The energy difference between them was fixed according to the reference characterization as were the relative centroid positions of $K\alpha_{12}$ and $K\alpha_{22}$. A parameter defines a constant low-energy background (rather than the linear or cubic value used in previous literature). The relative integrated intensities and FWHMs of this fit were tied to values given by the reference characterization. The source transfer was used from Hölzer *et al.* (1997), Illig *et al.* (2013) or Mendenhall *et al.* (2017) using the same methodology.

The Hölzer *et al.* (1997) characterization is high resolution and well separated for $K\alpha_1$ and $K\alpha_2$. Hence, relative integrated intensity ratios should be reliable, and transferable. The spectra were deconvolved with an unstated PSF which may yield model-dependent artefacts in the interpretation.

Illig *et al.* (2013) is based on a lower-resolution data set affected by characterized background effects, but might be most similar in instrumental broadening. This transfer standard provides the best χ^2_r for all spectra compared with Hölzer *et al.* (1997) or Mendenhall *et al.* (2017). The theoretical placement and magnitude of satellites should drive the integrated intensity ratio above 0.5. Limitations of the Illig *et al.* (2013) prescription include the slightly low integrated intensity ratio and the correlated low width and intensity of the $K\alpha_{12}$ component. Other parameters are plausible.

Mendenhall *et al.* (2017) is high resolution, may have involved a PSF deconvolution and used peculiar modelling and background functions. This relies on much more sophisticated instrumentation than the other two characterizations but also has larger systematic corrections as discussed therein.

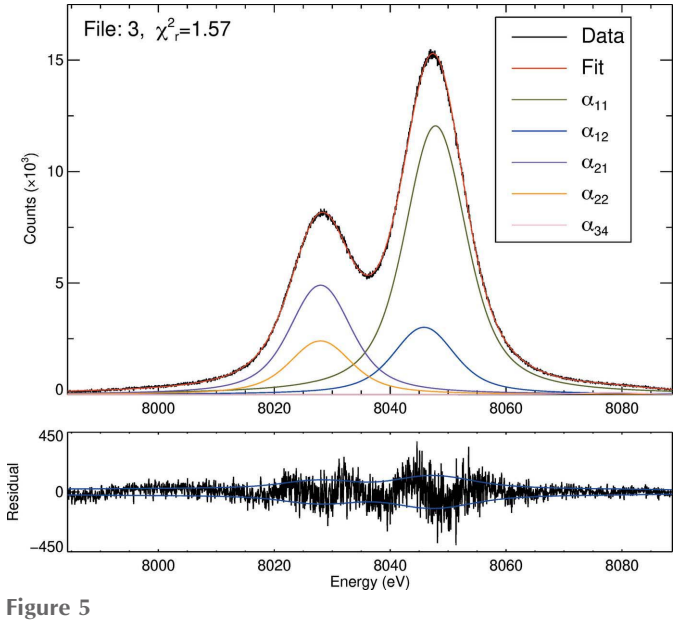

Figure 5
Peak-by-peak fit to the File 3 data set. The three spectra obtain similar fits in terms of components. However the relative size of $K\alpha_{12}$ changes across the three spectra, the component separations change accordingly, and the net asymmetry varies across the three spectra by this fitting approach.

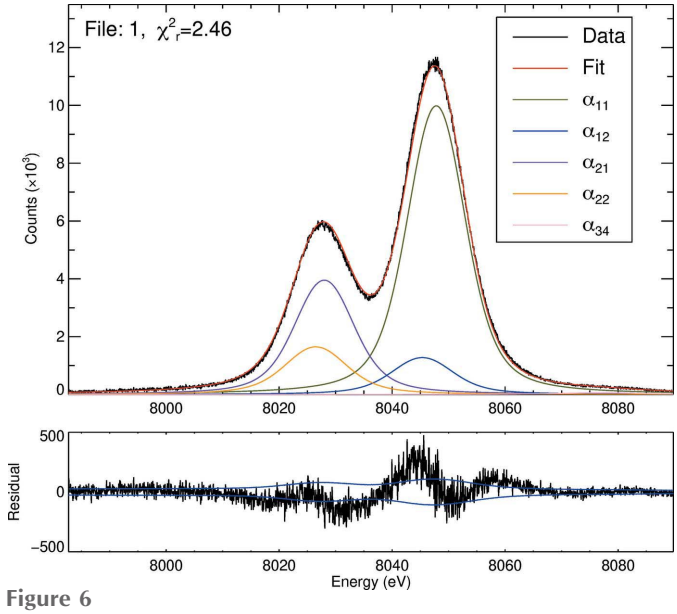

Figure 6
Use of Hölzer *et al.* (1997) as a transferable standard for the File 1 profile. Common Voigt broadening for the instrumental PSF was added to the sum of Lorentzians. The 2*p* satellite line parameters have been left free. The residual structure is typical for the Cu $K\alpha$ spectrum, but χ^2_r of 2.46 is a relatively poor fit.

A comparison of fits of the most sensitive spectrum is given in Figs. 6, 7 and 8, showing that the three characterizations are roughly consistent in general shape – the satellite lines are on the low-energy side of the dominating diagram lines and $K\alpha_{12}$ has a lower integrated intensity than $K\alpha_{22}$. In all cases, except for $K\alpha_{12}$ in Illig *et al.* (2013), the satellite lines have a greater FWHM than their corresponding diagram lines. These data sets and those previously published agree, again confirming the quality of the backgammon-type detector used. The residuals in each plot are typical of a four-component fit to a $K\alpha_{12}$ spectrum, indicating that the data presented here disagree with each of the fits in a similar fashion to the residuals in the original publications.

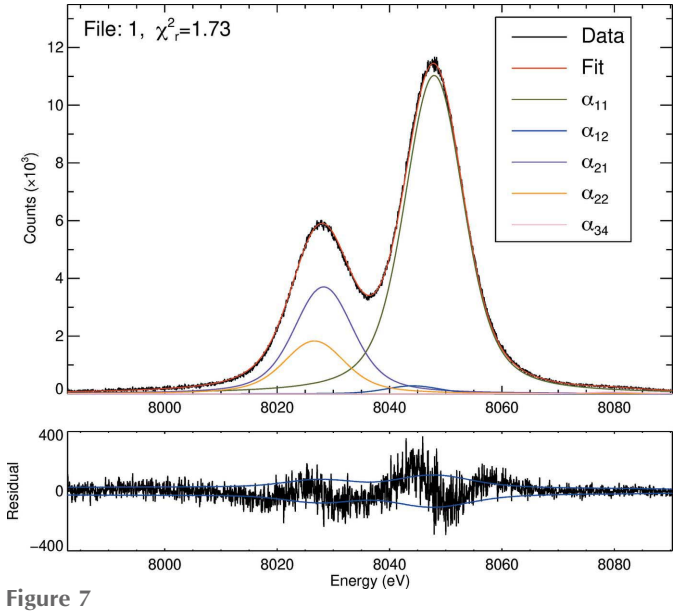

Figure 7
Use of Illig *et al.* (2013) as a transferable standard for the File 1 profile yielding the best fit, $\chi^2_r = 1.73$; however $I(K\alpha_2)/I(K\alpha_1) < 0.5$.

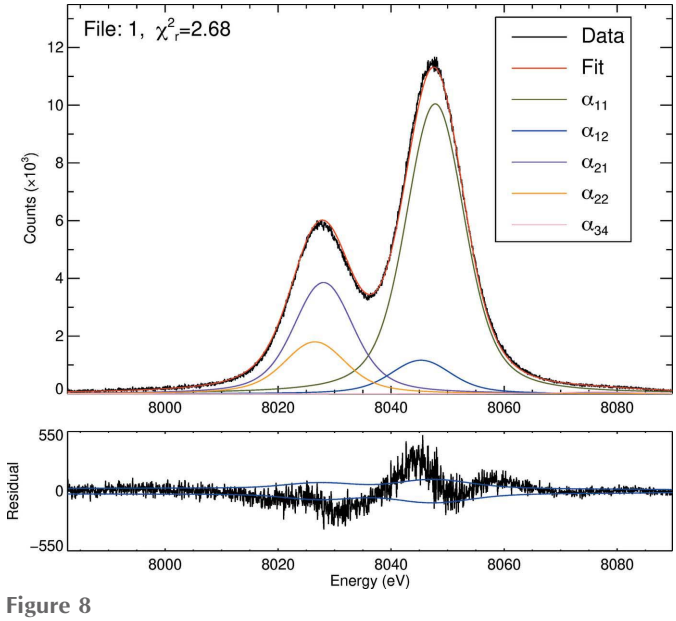

Figure 8
Use of Mendenhall *et al.* (2017) as a transferable standard for the File 1 profile. $\chi^2_r = 2.68$ is the highest and residuals are large.

8. Analysis: simultaneous constrained fit

As explained in Fig. 1, the literature characterizations are significantly different, reflected in the significant differences in χ^2_r and in the values being significantly higher than *e.g.* the peak-by-peak fits. The variation of residuals indicates the lack of direct portability of the data from one spectrum and measurement cycle to another, *i.e.* that the translation of the component representation has some potential systematic or unknown quantity. It is worth investigating a more reproducible component spectrum for copper $K\alpha$. This will invite further study and is challenging in general; however, we can make substantial progress here. The peak-by-peak approach failed to observe a valid integrated intensity ratio due to exchange of intensity between components compared with the literature parameterizations. One test of a fit is therefore to look at the integrated intensity ratio $I(K\alpha_2)/I(K\alpha_1)$ (Fig. 2). A value of less than 0.5 is possibly caused by broadening and correlated errors.

Fitting the raw data using a sum of Voigts can produce a fit as good or better than a fit produced by deconvolving the Gaussian PSF and then fitting the deconvolved spectrum with Lorentzians (Hölzer *et al.* (1997). However, the extra broadening makes it difficult to distinguish the $K\alpha_1$ components from $K\alpha_2$. The $[1s3d]^{-1} \rightarrow [2p_{1/2}3d]^{-1}$ transition may be partly modelled by $K\alpha_{12}$ rather than $K\alpha_{22}$, yielding a lower ratio of integrated intensities, $I(K\alpha_2)/I(K\alpha_1)$.

Mendenhall *et al.* (2017) and Hölzer *et al.* (1997) report $I(K\alpha_2)/I(K\alpha_1)$ of 0.521 (1) and 0.517 (20), respectively; our data suggest a ratio closer to the latter. Taking into account the uncertainty in the FWHM and intensity, the reported Hölzer *et al.* (1997) ratio could be consistent with 0.5098 or lower.

To ensure a physical fit, $I(K\alpha_2)/I(K\alpha_1)$ was set $\geq$0.51. Initially estimates are derived from the relevant characterization. The width of the satellite lines was tied to the diagram

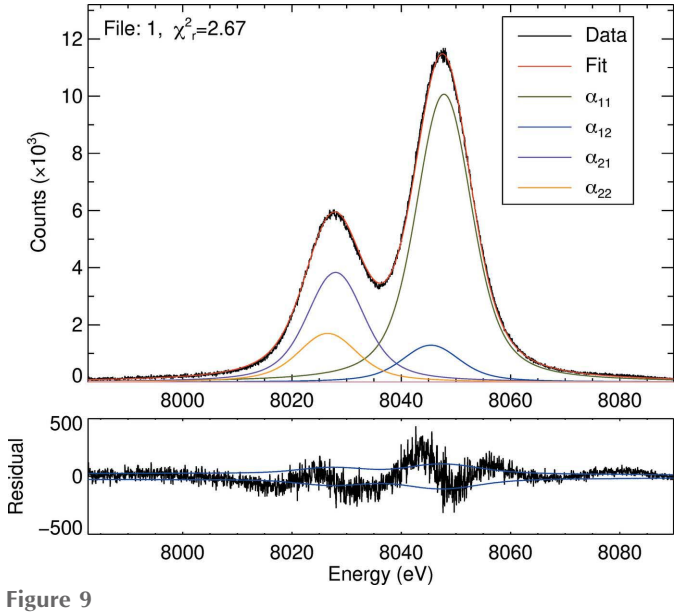

Figure 9
Simultaneous four-Voigt fit. The missing fifth peak around 8080 eV corresponds to $K\alpha_{3,4}$, the $2p$ satellite.

Table 4
Parameters of the simultaneous five-Voigt fit.

The $I(K\alpha_2)/I(K\alpha_1)$ ratio reached the constraint of 0.51 in the fitting procedure. The uncertainty in the ratio is derived from uncertainty in the integrated area. The uncertainty in the centroid energy is derived from the uncertainty in fitting and calibration of the energy scale. The satellite widths were loosely tied to the corresponding diagram line widths according to the literature (Hölzer *et al.*, 1997; Mendenhall *et al.*, 2017). $\chi_r^2 \simeq 2$ and the plausible integrated intensity ratio reflect an accurate and physically sound fit.

Channel size (eV)	Gaussian width (eV)	$I(K\alpha_2)/I(K\alpha_1)$ ratio	χ_r^2
0.059	3.931 (9)	0.510 (6)	2.071

Component	Energy (eV)	FWHM (eV)	Area (%)
$K\alpha_{11}$	8047.837 (5)	2.261 (28)	58.139 (285)
$K\alpha_{12}$	8045.433 (5)	2.804 (34)	7.723 (132)
$K\alpha_{21}$	8027.993 (8)	2.707 (32)	22.920 (178)
$K\alpha_{22}$	8026.566 (8)	3.305 (39)	10.670 (180)
$K\alpha''$	8077.491 (356)	9.869	0.549 (19)

line width according to Hölzer *et al.* (1997), Mendenhall *et al.* (2017). To emphasize the importance of the 2*p* satellite this approach was used to perform a four-Voigt fit (Fig. 9) and a five-Voigt fit (Fig. 10). The residual of Fig. 9 shows that the fit is adequate except for discrepancies around 8080 eV. This is the $[1s2p]^{-1} \rightarrow [2p]^{-2}$ process related to the 2*p* satellite.

The inclusion of a fifth Voigt at this peak more closely models the full spectrum, and results in a lower χ_r^2 (Fig. 10). This feature is a number of transitions centred around 8080 eV (Diamant *et al.*, 2006). Because of correlations between the width and integrated area parameters, the width of the 2*p* satellite is constrained to 9.868 eV to minimize both the χ_r^2 and discrepancies from Mendenhall *et al.* (2017). For this reason no

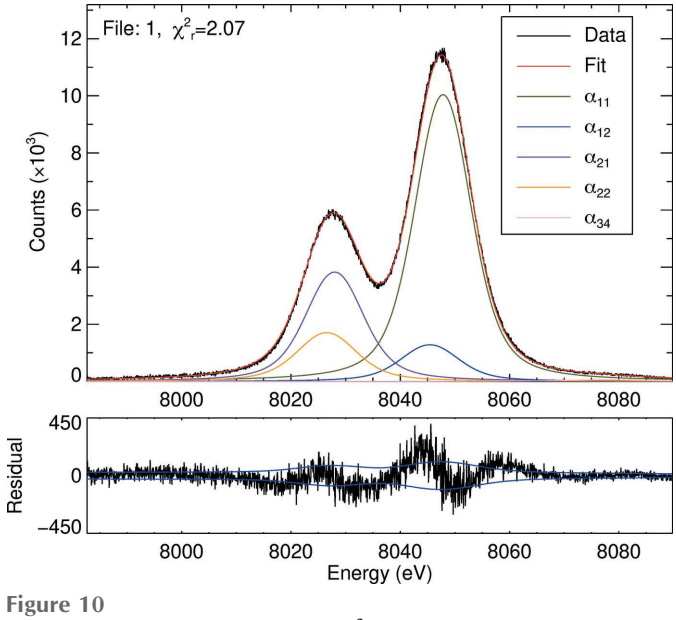

Figure 10
Simultaneous five-Voigt fit. The χ_r^2, when compared with Fig. 9, demonstrates the significance of the 2*p* satellite, the $[1s2p]^{-1} \rightarrow [2p]^{-2}$ transition. The inclusion of this peak can be seen through comparing the residual around 8080 eV of this figure and Fig. 9.

Table 5
Comparison of results of the peak-by-peak fitting approach, attempts to transfer the prior characterizations as standards directly, and the simultaneous fit for each of the spectra.

$I(K\alpha_2)/I(K\alpha_1)$ is the integrated intensity ratio, expected to be greater than 0.51 on the basis of the literature.

Spectrum	File 1	File 2	File 3
Peak-by-peak fit			
χ_r^2	1.40	1.41	1.57
$I(K\alpha_2)/I(K\alpha_1)$	0.469 (6)	0.486 (10)	0.486 (4)
Transfer of standard (Hölzer *et al.*, 1997)			
χ_r^2	2.46	2.06	2.25
$I(K\alpha_2)/I(K\alpha_1)$	0.517 (20)	As above	As above
Transfer of standard (Illig *et al.*, 2013)			
χ_r^2	1.73	1.57	1.73
$I(K\alpha_2)/I(K\alpha_1)$	0.498 (6)	As above	As above
Transfer of standard (Mendenhall *et al.*, 2017)			
χ_r^2	2.68	2.25	2.45
$I(K\alpha_2)/I(K\alpha_1)$	0.521 (2)	As above	As above
Simultaneous fit			
χ_r^2	2.07	1.80	1.96
$I(K\alpha_2)/I(K\alpha_1)$	0.510 (6)	As above	As above

uncertainty is quoted for this width. The parameters of this fit (Table 4) represent our best characterization of the Cu $K\alpha$ spectrum, are comparable with what has been previously reported and can be tied to the physical processes in the spectra. The amplitudes have been normalized and the common Gaussian broadening term allowed to vary across the three data sets. χ_r^2 values for each of the data sets are shown in Table 4. This proves that modified modelling can achieve a reduced χ_r^2 while maintaining something close to the correct ratio. The current result appears to be a good transferable calibration.

9. Discussion

The characterization (Fig. 10, Table 4) has a χ_r^2 of 2.07 and $I(K\alpha_2)/I(K\alpha_1) = 0.51$. This fit is robust across all spectra and improved compared with that of Hölzer *et al.* (1997), Mendenhall *et al.* (2017) (Table 5). Because of this, the characterization of the spectrum is transferable to un-broadened spectra and relatable to physical processes.

Our results can be interpreted to give insight into the atomic processes present. In particular, these results support a 2*p* satellite width close to 10 eV, as suggested by Mendenhall *et al.* (2017). It suggests a centroid location for the 2*p* satellite which is lower than that given by Fritsch *et al.* (1998), Mendenhall *et al.* (2017) but higher than that given by Illig *et al.* (2013), and this may be dependent upon the details of the background treatment or the background flux. It assumes an intensity ratio fully consistent with that of Illig *et al.* (2013), Hölzer *et al.* (1997) yet lower than that of Mendenhall *et al.* (2017). All widths and centroids are plausible so that the

Table 6
Difference in parameters between our results and those of Mendenhall *et al.* (2017).

The lower panel shows the difference as a fraction of the sum of 1σ (standard errror) uncertainties. As our measurement is a relative one, rather than an absolute, the energy scale has been shifted in order for the energy of $K\alpha_{11}$ to match that of Mendenhall *et al.* (2017).

Component	Energy (eV)	FWHM (eV)	Area (%)
$K\alpha_{11}$	0.000	0.014	−0.163
$K\alpha_{12}$	0.126	−0.111	0.655
$K\alpha_{21}$	−0.069	0.178	0.106
$K\alpha_{22}$	0.016	0.031	−0.573
Shifts with respect to parameter standard errors			
$K\alpha_{11}$	0.000σ	−0.475σ	−0.509σ
$K\alpha_{12}$	13.535σ	−2.562σ	3.954σ
$K\alpha_{21}$	−6.548σ	4.757σ	0.348σ
$K\alpha_{22}$	0.928σ	0.656σ	−1.867σ

Table 7
Difference in parameters between our results and those published by Hölzer *et al.* (1997).

The lower panel shows the difference as a fraction of the sum of 1σ (standard errror) uncertainties. Notice that our results match those of Hölzer *et al.* (1997) more closely than those of Mendenhall *et al.* (2017).

Component	Energy (eV)	FWHM (eV)	Area (%)
$K\alpha_{11}$	0.000	−0.024	0.239
$K\alpha_{12}$	0.066	−0.554	−0.277
$K\alpha_{21}$	0.000	0.041	−0.680
$K\alpha_{22}$	0.062	−0.266	0.170
Shifts with respect to parameter standard errors			
$K\alpha_{11}$	0.000σ	−0.771σ	0.621σ
$K\alpha_{12}$	2.484σ	−9.327σ	−1.198σ
$K\alpha_{21}$	0.000σ	1.033σ	−2.449σ
$K\alpha_{22}$	2.850σ	−4.254σ	0.607σ

anomalous width of $K\alpha_{12}$ of Illig *et al.* (2013) is addressed. The centroids of the four main peaks are mainly consistent with Hölzer *et al.* (1997) to a few standard errors but somewhat inconsistent with Mendenhall *et al.* (2017). The χ^2_r are superior to the application of Hölzer *et al.* (1997), Mendenhall *et al.* (2017) but inferior to the application of Illig *et al.* (2013) and that of the peak-by-peak approach. The component area intensities are quite close to but distinct from those of Hölzer *et al.* (1997), Mendenhall *et al.* (2017). The differences between our parameters and those of Mendenhall *et al.* (2017) and Hölzer *et al.* (1997) are shown in Tables 6 and 7.

The shake probabilities, well above threshold, are a function of Z. We report a 3d shake probability of 18.39 (22)%, fully consistent with the values given by Hölzer *et al.* (1997) and Mendenhall *et al.* (2017) of 18.31 (13)% and 18.5 (1)%; and higher than the value of Illig *et al.* (2013) of 12.6 (1)%. Typically, theoretical determination of shake probabilities has been lower than those values found experimentally (Lowe *et al.*, 2011; Mukoyama & Taniguchi, 1987; Kochur *et al.*, 2002) (see Table 8). Neither Holzer nor Mendenhall explicitly tie the satellite intensity to a shake probability. However, the integrated intensity of the $K\alpha_{12}$ and $K\alpha_{22}$ lines is a measure of hole creation through shake events (Ito *et al.*, 2016).

Table 8
The 3d shake probabilities calculated through theory and through fitting to experimental data.

Large discrepancies between theory and experiment remain.

	3d shake probability (%)
Theory	
Mukoyama & Taniguchi (1987)	9.7
Kochur *et al.* (2002)	14.5
Lowe *et al.* (2010)	14.7
Experiment	
Deutsch *et al.* (1995)	30.0
Hölzer *et al.* (1997)	18.5 (1)
Galambosi *et al.* (2003)	25 (2)
Enkisch *et al.* (2004)	20.0
Ito *et al.* (2006)	23.1
Chantler *et al.* (2009)	29.0 (25)
Chantler *et al.* (2010)	26.0
Illig *et al.* (2013)	12.6 (1)
Mendenhall *et al.* (2017)	18.31 (13)
This work	18.39 (22)

Table 9
The shake probabilities, both experimental and theoretical, for the 2p electron.

Here there is less discrepancy but also fewer results found in the literature.

	2p shake probability (%)
Theory	
Mukoyama & Taniguchi (1987)	0.465
Experiment	
Illig *et al.* (2013)	0.215 (1)
Mendenhall *et al.* (2017)	0.574 (12)
This work	0.549 (19)

The 2p satellite line, $K\alpha_{3,4}$, is due to a 2p spectator vacancy: $[1s2p]^{-1} \rightarrow [2p]^{-2}$. Our 2$p$ satellite line gives a contribution of 0.00549 (19), *i.e.* a shake probability of 0.549 (19)%. This is fully consistent with the experimental value given by Mendenhall *et al.* (2017) and closer to the theoretical value found by Mukoyama & Taniguchi (1987) than either those of Illig *et al.* (2013) or Mendenhall *et al.* (2017) (Table 9).

Another measure often used to compare line shapes is the index of asymmetry or asymmetry index (AI). The AI is the ratio of the half width at half-maximum on the low- and high-energy side of each peak. While the AI is relatively easy to extract when comparing experimental results, it primarily indicates an experimental trend, error or variation, and is strongly subject to resolution and instrumental broadening.

The values are a strong functional of broadening (Hölzer *et al.*, 1997). To eliminate confusion in comparisons, caused by broadening, we report AIs given by the un-broadened parameterization. For consistency, the AIs given in Table 10 that have been calculated by us (final row, 'This work') have also been obtained using the parameterization. This means we are comparing the parameterization, which should be transferable, rather than the data, which will in general be dependent on broadening and experimental setup.

We report an AI for the $K\alpha_1$ line of 1.06 and 1.34 for $K\alpha_2$, extremely similar to that of Hölzer *et al.* (1997). The AI of the

Table 10
Comparison of Cu $K\alpha$ quantifications across the literature.

FWHM shows the Lorentzian FWHM, AI is the asymmetry index of each peak and $I(K\alpha_2)/I(K\alpha_1)$ is the integrated intensity ratio.

	FWHM (eV)		AI		
	$K\alpha_1$	$K\alpha_2$	$K\alpha_1$	$K\alpha_2$	$I(K\alpha_2)/I(K\alpha_1)$
Parratt (1936*b*)	2.40	3.31	1.15	1.28	
Salem & Wimmer (1970)					0.508
Berger (1986)	2.41	3.39	1.08	1.36	0.478
Sorum (1987)	2.28 (5)	2.78 (5)	1.11 (5)	1.34 (3)	0.52
Deutsch *et al.* (1995)†	2.42	3.41	1.08	1.34	0.53
Hölzer *et al.* (1997)	2.35	3.41	1.07	1.36	0.517 (20)
Illig *et al.* (2013)‡	2.43	3.47	1.00	1.58	0.498 (6)
Mendenhall *et al.* (2017)‡	2.324	3.287	1.060	1.450	0.520 (2)
This work (un-broadened)	2.333	3.391	1.093	1.371	0.510 (6)

† Double-crystal results from Deutsch *et al.* (1995). ‡ Indicates the quantification has been calculated by us, rather than reported in the paper.

Table 11
The AIs, FWHM and integrated peak ratio of the Sc $K\alpha$ spectrum as reported in the literature.

Estimated errors, where available, are shown in parentheses.

	FWHM (eV)		AI		
Scandium, Sc, $Z = 21$	$K\alpha_1$	$K\alpha_2$	$K\alpha_1$	$K\alpha_2$	$I(K\alpha_2)/I(K\alpha_1)$
Anagnostopoulos *et al.* (1999)	1.332 (16)	1.744 (28)	1.113 (17)	0.884 (16)	0.52
Chantler *et al.* (2006)	1.271	1.691	1.082	0.917	0.512
Ito *et al.* (2016)	1.243 (15)	1.358 (49)	1.060 (14)	0.869 (8)	0.525 (4)
Dean *et al.* (2019)	1.242 (76)	1.521 (176)	1.068 (7)	0.934 (12)	0.503 (25)

$K\alpha_2$ reported by Mendenhall *et al.* (2017) is larger than other values due to the larger relative size of the satellite contribution. The parameterization of Illig *et al.* (2013) gives an AI for $K\alpha_1$ significantly smaller than others due to the smaller integrated intensity of the $K\alpha_1$ components. Similarly, the larger AI for $K\alpha_2$ is explained by a large energy difference between the diagram and satellite line and the large satellite contribution.

The FWHMs of each of the two peaks present in the spectrum are also used to compare experimental results and trends with Z across X-ray spectra. Typically, the FWHM of interest is the FWHM of the un-broadened spectrum, obtained through deconvolution of the measured or *observed* spectrum.

A double crystal will, in general, result in a less broad spectrum and hence lower values for the FWHMs. It is interesting then that the parameterization given by Hölzer *et al.* (1997), obtained using a single crystal, gives smaller FWHMs than that of Deutsch *et al.* (1995), obtained with a double crystal. The double crystal used by Parratt (1936*b*) explains their slightly lower value for the $K\alpha_2$ FWHM.

Parratt (1936*b*) provides a detailed analysis of the $K\alpha_{3,4}$ lines, which can be compared with the results of Fritsch *et al.* (1998), Mendenhall *et al.* (2017).

Sorum (1987) uses a two-Lorentzian model to fit the data rather than the more common four or five Lorentzians, and yields a much lower FWHM. While other models are also reported in the work of Sorum (1987) none give a transferable parameterization that can be reproduced and compared. Berger (1986) provides an excellent fit to their data using the simple four-Lorentzian model. The FWHMs of both the spectrum obtained and the individual components agree closely with our own. Why the $I(K\alpha_2)/I(K\alpha_1)$ value is below 0.5 is not discussed in the paper nor obvious.

The intensity ratio is consistent with all literature except Mendenhall *et al.* (2017). It is instructive to consider this in relation to the range across the periodic table, Fig. 2, and the beginning of the transition metals, Sc, $Z = 21$, as a baseline (Table 11) together with the FWHM and AI. We would expect the component ratio to be less for Sc than for Cu and this is true from the recent determination by Dean *et al.* (2019). However, the uncertainties imply further work is needed to confirm the theoretically expected pattern, and past literature fails to clarify or define a pattern. The Cu spectrum is significantly broader than the Sc spectrum, with an FWHM almost double that for Sc for both peaks. However, the fine structure implies that the peak separation for Cu is of the order of 20 eV, much larger than that of 5 eV for Sc, so that the components can be more clearly separated for Cu. Because of the positions of satellite lines the AI for $K\alpha_2$ changes from below unity, for Sc, to above 1, in the Cu spectrum. The AIs for $K\alpha_1$ are relatively similar. Both are in good agreement with Fig. 5 of Ito *et al.* (2016). The interpretation and significance of this are not yet understood, but may relate to the need for advanced theoretical computation of different satellite structure and magnitude across the transition metals, which are known to have a strong Z dependence.

10. Conclusion

The results presented above demonstrate the robustness of the five-Voigt characterization of the Cu $K\alpha$ spectrum, the method of fitting, and its link to the simpler but inadequate four-component sum reported in the literature. The Voigt method requires little knowledge of the instrumental function. However, care must be taken to obtain parameters transferable to all resolutions and representing the physical atomic processes. The characterization of the spectra obtained *is* dependent on the approach. The RA approach and the peak-by-peak approach gave reasonable fits to the data, but failed to generate plausible and robust components linked to physical processes. The re-characterization of previous empirical fits confirmed our data were consistent with what has been reported in the literature and the simultaneous constrained approach improved upon these parameterizations. The copper characterization has been a benchmark for

all X-ray spectroscopy and spectroscopic calibration, together with edge energies, and therefore remains a major focus of the high-accuracy and theoretical X-ray and crystallographic communities.

Our final characterization is broadly consistent with previous literature. The AI and FWHM are comparable with most other characterizations. We report a 3*d* shake probability of 18.39 (22)%, consistent with the best previous characterizations, and a 2*p* shake probability of 0.549 (19)%.

In answering our four critical questions from Section 1, the excellent prior characterizations currently appear inconsistent with one another, which might depend upon source, background, optic or detection methods. They are robust and remain useful, but the discrepancies must be addressed in future work, and are partly addressed in terms of transferability in this work. Differences in some parameters of the current characterizations – including our own – do approach the 1 p.p.m. level. At the moment the two or three best characterizations differ in components by many per cent and standard errors. Equally they do not apply in a cross-platform portable manner. Particularly, the large discrepancy of the satellite shape and structure is a cause for strong concern. For the purpose of calibration the most important discrepancies are the $K\alpha_{1,2}$ peak energies as these are often used to define the energy scale. At present the inconsistencies between these peaks are on the order of 10 p.p.m. Ideally, the standard should be improved until the characterization is stable across experiment (within error) so that theory and experiment on different X-ray sources under defined conditions would yield the same spectra. Looking at Tables 7, 6 and 2 this is clearly not the case at present. Resolving these inconsistencies to the 1 p.p.m. level will no doubt lead to advances in both experiment and atomic theory.

For theoreticians, we look to be able to compute relativistic quantum mechanical theory to agree with the experimental spectra and with the platform-independent characterization, but this is not yet possible. Increasing accuracy to the 1 p.p.m. level will make testing relativistic quantum mechanical theory possible.

While it may sound like an extreme stretch goal, these characteristic X-ray spectra contain large contributions from quantum electrodynamics (QED) and hence may afford the possibility of new tests and confirmation (or otherwise) of QED in atomic and metallic systems, which are currently not feasible.

We have obtained a novel characterization of the spectra, which raises questions relating to the best two prior works including a question of robustness, and a counterpoint for future comparisons with standard sources and geometries. In particular, the new characterization naturally includes an instrumental broadening including an additional Voigt profile which will represent a range of common laboratory experiments. The study of robustness and stability of the detailed spectra must continue. In the meantime, the methodology discussed herein might be required for future calibration exercises and investigations of the robustness and characterization of copper $K\alpha$ spectra; the methodology can also apply to other characteristic radiation less well studied than copper $K\alpha$.

Our final result provides a parameterization suitable for calibration purposes in other experiments and for testing theoretical calculations and predictions across a range of atomic processes. To obtain a more complete understanding of X-ray spectra, further work should involve a deeper experimental investigation across a wide range of geometries. We have confirmed that the $K\alpha$ doublet can be well modelled by the sum of five spectral components. $\chi^2_r \simeq 2$ models the data well and apparently robustly.

We know theoretically that there is further substructure within both the satellite and diagram lines. Five-component Voigts are robust and applicable to a wide range of experimental geometries and are required by the quality of our data. The multiplet substructure of the satellite and diagram lines can be further investigated through theoretical calculations using multi-configuration Dirac–Hartree–Fock (MCDHF) (Chantler, Lowe & Grant, 2012; Deutsch *et al.*, 2004).

APPENDIX *A*
Experimental details

Full details of the experimental design and detector can be found in the work of Melia *et al.* (2019). Here we explain key details specific to the Cu spectrum.

The attenuators were a series of 12 µm aluminium foils, with negligible energy dependence across the energy of the spectrum. Their absorption is well defined, with no edge in the region, and the analysis does not depend upon detailed accurate roughness or sample characterization, as we have done in other work.

The satellite lines' integrated intensities are tied to shake processes, the probability of which should change with accelerating voltage. At some voltage the spectrum will stabilize and the probabilities of shake events reach a maximum. This plateau voltage has previously been shown to be less than the accelerating voltage used here of 20 kV (Illig *et al.*, 2013; Deutsch *et al.*, 2004). In similar situations, from 20 to 50 kV 'the profile is stable to the noise limit' (Illig *et al.*, 2013). Several of these past works use 40 kV, and 20 to 50 kV; this current work uses 20 kV. Hence this is sufficient for the spectra to be stable in the sudden impact spectral distribution. In other words, these excitation conditions should yield a stable experimental transferable standard.

Background subtraction in these characterizations often uses a constant or linear function, and a cubic in earlier characterizations (Mendenhall *et al.*, 2017). Conversely, in this study, we characterize the background by heavily attenuated foils, thus suppressing the main spectrum and revealing components from the electronic noise, higher harmonics and any stray beams; these correct the background structure in the beam very effectively. This is demonstrated and proven by the simplicity and flatness of the consequent spectra. Note that the background-corrected spectrum goes to zero at both ends of the spectrum.

Table 12
Three data sets plus a background measurement.

The three data sets differ in the attenuation between detector and source. The frequency column shows the count rate at which X-ray events were measured by the detector.

	No. foils	Exposure time (s)	Current (mA)	Total counts	Frequency Hz count rate
File 1	32	7200	14	6553428	910.2
File 2	24	7200	10	8339156	1158.2
File 3	24	7200	10	8343119	1158.8
Background	104	1200	200	1506841	1255.7

APPENDIX *B*
Fitting function

The function used to model the spectrum is the sum of five Voigt functions and background parameters $B(E)$:

$$f(E) = \sum_{i=1}^{5} V_i(E; \gamma_i, \sigma, E_i, A_i) + B(E) \quad (1)$$

where the ith Voigt is given by

$$V_i(E; \gamma_i, \sigma, E_i, A_i) = \frac{A_i}{\sigma(2\pi)^{1/2}} \int_{-\infty}^{\infty} \frac{\gamma_i \exp[-x^2/(2\sigma^2)]}{\pi[(E - E_i - x)^2 + \gamma_i^2]}\, dx \quad (2)$$

and γ_i is the Lorentzian broadening parameter (γ is the half width at half-maximum of the Lorentzian or FWHM/2), E_i is the centroid position and A_i is the integrated area of the Lorentzian. The Gaussian broadening parameter, σ, represents the common instrumental broadening.

The profiles collected (Table 12) differ in the attenuation between the detector and source, the current applied to the rotating anode, the time of the exposure and the count-rate recorded by the detector. For each of the approaches to analysis, each profile has been fitted using the same Levenberg–Marquardt fitting technique. The goodness of fit is characterized by χ_r^2:

$$\chi_r^2 = \frac{\chi^2}{N} \quad (3)$$

where N is the number of degrees of freedom, in our case the number of fitted data points plus the number of fitting parameters. When fitting, an effort has been made to ensure that the global minimum is found capturing the physical processes rather than an unphysical local minimum; hence some parameters, at times, were constrained. The energy scale on these figures and used to convert channels to eV has been calibrated using the work of Hölzer *et al.* (1997), specifically the energies of the $K\alpha_{11}$ and $K\alpha_{21}$ components of 8047.8369 and 8027.9932 eV. The uncertainty in the number of counts in each channel of the detector was in our case very close to Poissonian [$\Delta I_i = (I_i)^{1/2}$].

APPENDIX *C*
Residual component analysis results

The results of this technique are shown in Figs. 11 and 12 for four- and five-Voigt models, respectively. The parameters for Fig. 12 are displayed in Table 13.

Although the fit with five components has $\chi_r^2 = 1.33$, and the F-test implies a much superior model than the four-Voigt fit ($\Delta\chi^2 = 0.43$), this approach has several limitations. Firstly the RA, while relatively robust, will not always work because, in general, the residual profile is extremely noisy and complex. Such an analysis is more suited to high-resolution data where the residuals have more separable structure. Leaving all parameters free often yields a fit with multiple Voigts centred at the same position, meaning one transition is represented by two Voigts, or that the double asymmetric peak attempts to be modelled by two separated width components, for the peak and for the tails independently. Because the correlation is high, there is a tendency for the fit to give subsequent Voigts an amplitude of zero, yielding a false and poor apparent minimum. Hence, in the current approach, amplitudes have been constrained to be nonzero and Lorentzian broadening has also been limited. The RA yielded quite variable fits across the three data sets, *i.e.* they were neither robust nor inconsistent, so does not represent a plausible characterization. The four-Voigt fit yielded centroids closer to Hölzer *et al.* (1997) than the five-Voigt fit which, while fitting the last peak, found a different local minimum to the four-Voigt. Comparison of Figs. 11 and 12 demonstrates this for the File 1 data set.

To improve the results given by the five-Voigt RA, another modified approach was attempted. An extra Voigt was added to the four-Voigt fit but in this case the parameters of the first

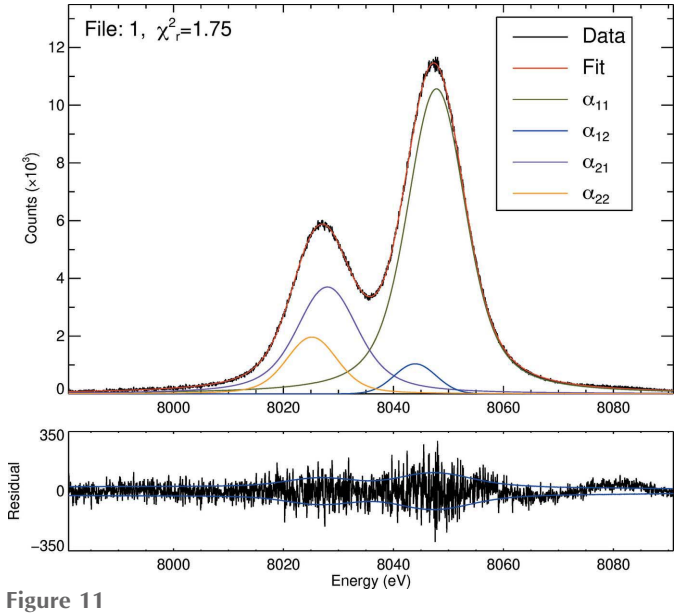

Figure 11
A four-Voigt fit using a residual analysis approach. These parameters match those of Hölzer *et al.* (1997) more closely than the following five-Voigt fit, especially the size of $K\alpha_{12}$. In this fit the $2p$ satellite is unaccounted for so the χ_r^2 is relatively large. The residuals illustrate that the fit fails around the $2p$ satellite, 8080 eV.

Table 13
The parameters given by the residual analysis approach, for the File 1 data set, using a five-Voigt fit.

The RA is poor with low widths in the satellites because the dominant two components are not well separated from the satellite locations. Although this method can work moderately well with high-resolution data it is not well suited to standard instrumental broadening. In essence, it finds poor estimates for the subsequent component and the fit is then too correlated to locate an optimized minimum.

Channel size (eV)	Gaussian width (eV)	$I(K\alpha_2)/I(K\alpha_1)$	χ_r^2
0.059	4.209	0.514	1.324

Component	Energy (eV)	FWHM (eV)	Area (%)
$K\alpha_{11}$	8047.837	6.427	51.792
$K\alpha_{12}$	8046.454	0.630	14.088
$K\alpha_{21}$	8027.993	8.885	20.901
$K\alpha_{22}$	8026.537	1.754	12.948
$K\alpha''$	8079.671	2.089	0.271

four Voigts were held fixed, allowing the program to find a fit for the fifth extra peak without disturbing the fit found earlier. The inclusion of this extra peak gives a better fit and lower χ_r^2. Further improvement was accomplished by next allowing the parameters of the original four Voigts to vary within constraints with the minimum found similar to that for the four-Voigt fit. The first four Voigts were constrained to be within 5% of the original four-Voigt fit (Fig. 13). Table 14 shows the parameters of this fit. The general structure of these components is comparable with what has been found in the literature (Illig *et al.*, 2013). However the Lorentzian FWHMs

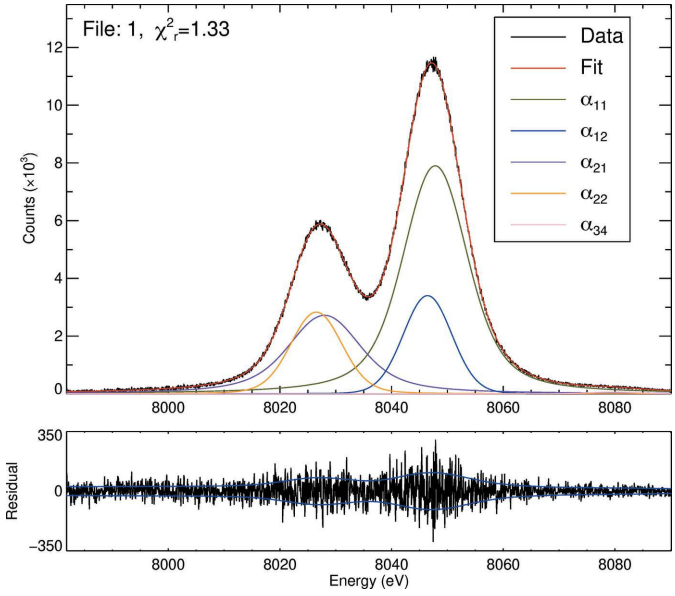

Figure 12
A five-Voigt fit given by the residual analysis approach. The parameters of this fit do not match those of Hölzer *et al.* (1997) and the satellite locations are near-degenerate with the dominant components. The fifth Voigt peak (Table 13) only has an integrated intensity of ∼0.3%. However its inclusion is necessary by comparison with Fig. 11. Residual discrepancies are mainly in the tail regions.

Table 14
Parameters from an RA approach, for the File 1 data set, using the constrained five-Voigt fit (Fig. 13).

Some parameters have no uncertainty, having reached the constraint in the fitting procedure, and hence are not robust.

Channel size (eV)	Gaussian width (eV)	$I(K\alpha_2)/I(K\alpha_1)$	χ_r^2
0.059 (3)	3.969 (42)	0.492	1.338

Component	Energy (eV)	FWHM (eV)	Area (%)
$K\alpha_{11}$	8047.837 (60)	5.821	63.187 (293)
$K\alpha_{12}$	8045.297 (463)	0.064	3.713
$K\alpha_{21}$	8027.993 (124)	6.644	23.181 (884)
$K\alpha_{22}$	8026.369 (258)	3.322	9.706 (0)
$K\alpha''$	8080.212 (188)	0.835 (333)	0.213 (12)

of this fit are inconsistent, with satellite widths smaller than the diagram lines.

The RA approach has been used to obtain fits with low χ_r^2 yet often generates components that are too narrow, unphysical or with zero amplitudes. Previous use of this approach has found components of physical significance even with a free fit (Illig *et al.*, 2013). However, for modelling this data set, the parameters required constraint to find plausible components. The determined $I(K\alpha_2)$:$I(K\alpha_1)$ ratio obtained was often less than 0.50, remembering the expectation of this being above 0.50. While further optimization is possible we consider improved alternative approaches in the text.

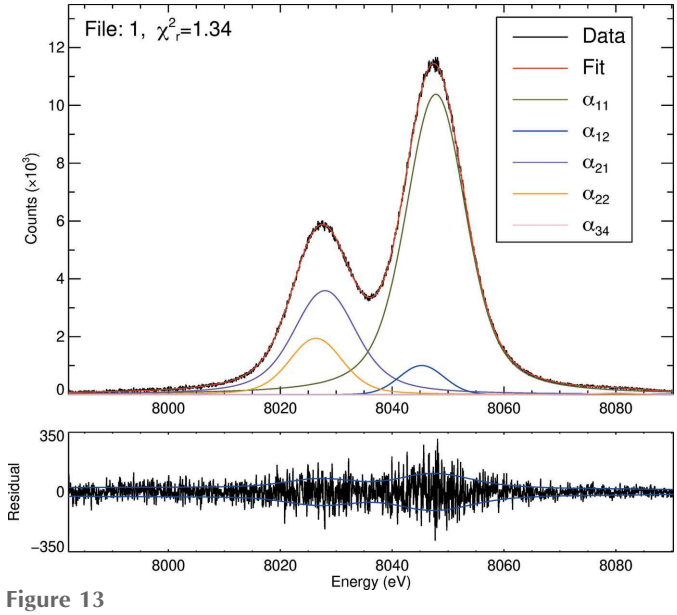

Figure 13
The first four Voigt parameters have been allowed to vary by ±5% to ensure the minimum found was similar to that for the four-Voigt fit. While the χ_r^2 is equivalent to that of Fig. 12, the parameters are more meaningful. This is the best result obtained using the RA approach with $\chi_r^2 \simeq 1$ and the general structure of the components resembling that in the literature. The satellite peaks are on the low-energy side of the diagram lines as expected and of similar relative integrated intensity to predictions. However, it illustrates the high correlation of parameters in fitting and the difficulty of generating a unique characterization.

Acknowledgements

We acknowledge A. T. Payne for his part in the data acquisition and design of the backgammon detector. We acknowledge the group of X-ray and synchrotron science at the School of Physics.

References

Anagnostopoulos, D., Sharon, R., Gotta, D. & Deutsch, M. (1999). *Phys. Rev. A*, **60**, 2018–2033.
Armelao, L., Bottaro, G., Pascolini, M., Sessolo, M., Tondello, E., Bettinelli, M. & Speghini, A. (2008). *J. Phys. Chem. C*, **112**, 4049–4054.
Berger, H. (1986). *X-ray Spectrom.* **15**, 241–243.
Chantler, C. T., Hayward, A. C. L. & Grant, I. P. (2009). *Phys. Rev. Lett.* **103**, 2–5.
Chantler, C. T., Kinnane, M. N., Gillaspy, J. D., Hudson, L. T., Payne, A. T., Smale, L. F., Henins, A., Pomeroy, J. M., Tan, J. N., Kimpton, J. A., Takacs, E. & Makonyi, K. (2012). *Phys. Rev. Lett.* **109**, 1–5.
Chantler, C. T., Kinnane, M. N., Su, C. & Kimpton, J. A. (2006). *Phys. Rev. A*, **73**, 012508.
Chantler, C. T., Lowe, J. A. & Grant, I. P. (2010). *Phys. Rev. A At. Mol. Opt. Phys.* **82**, 052505.
Chantler, C. T., Lowe, J. A. & Grant, I. P. (2012). *Phys. Rev. A At. Mol. Opt. Phys.* **85**, 032513.
Crasemann, B. (1987). *J. Phys. Colloq.* **48**(C9), C9-389–C9-400.
Dean, J. W., Chantler, C. T., Smale, L. F. & Melia, H. A. (2019). *J. Phys. B*. Submitted.
Deutsch, M., Förster, E., Hölzer, G., Härtwig, J., Hämäläinen, K., Kao, C. C., Huotari, S. & Diamant, R. (2004). *J. Res. Natl Inst. Stand. Technol.* **109**, 75–98.
Deutsch, M., Hölzer, G., Härtwig, J., Wolf, J., Fritsch, M. & Förster, E. (1995). *Phys. Rev. A*, **51**, 283–296.
Diamant, R., Huotari, S., Hämäläinen, K., Sharon, R., Kao, C. C. & Deutsch, M. (2006). *Radiat. Phys. Chem.* **75**, 1434–1446.
Diamant, R., Huotari, S., Hämäläinen, K., Sharon, R., Kao, C. C. & Deutsch, M. (2009). *Phys. Rev. A At. Mol. Opt. Phys.* **79**, 062511.
Doniach, S. & Sunjic, M. (1970). *J. Phys. C Solid State Phys.* **3**, 285–291.
Enkisch, H., Sternemann, C., Paulus, M., Volmer, M. & Schülke, W. (2004). *Phys. Rev. A*, **70**, 022508.
Fritsch, M., Kao, C. C., Hämäläinen, K., Gang, O., Förster, E. & Deutsch, M. (1998). *Phys. Rev. A*, **57**, 1686–1697.
Galambosi, S., Sutinen, H., Mattila, A., Hämäläinen, K., Sharon, R., Kao, C. C. & Deutsch, M. (2003). *Phys. Rev. A*, **67**, 022510.
Gillaspy, J. D., Chantler, C. T., Paterson, D., Hudson, L. T., Serpa, F. G. & Takács, E. (2010). *J. Phys. B At. Mol. Opt. Phys.* **43**, 074021.
Hansen, S. B., Faenov, A. Y., Pikuz, T. A., Fournier, K. B., Shepherd, R., Chen, H., Widmann, K., Wilks, S. C., Ping, Y., Chung, H. K., Niles, A., Hunter, J. R., Dyer, G. & Ditmire, T. (2005). *Phys. Rev. E Stat. Nonlin. Soft Matter Phys.* **72**, 036408.
Härtwig, J., Hölzer, G., Wolf, J. & Förster, E. (1993). *J. Appl. Cryst.* **26**, 539–548.
Hölzer, G., Fritsch, M., Deutsch, M., Härtwig, J. & Förster, E. (1997). *Phys. Rev. A*, **56**, 4554–4568.
Illig, A. J., Chantler, C. T. & Payne, A. T. (2013). *J. Phys. B At. Mol. Opt. Phys.* **46**, 235001.
International Tables for Crystallography (2019). Vol. C, edited by T. R. Welberry, ch. 4.2. 4th ed., in the press. Chichester: Wiley.
Ito, Y., Tochio, T., Ohashi, H., Yamashita, M., Fukushima, S., Polasik, M., Słabkowska, K., Syrocki, Ł. & Szyma, E. (2016). *Phys. Rev. A*, **94**, 042506.
Ito, Y., Tochio, T., Oohashi, H. & Vlaicu, A. M. (2006). *Radiat. Phys. Chem.* **75**, 1534–1537.
Kawai, J., Konishi, T., Shimohara, A. & Gohshi, Y. (1994). *At. Spectrosc.* **49**, 725–738.
Kochur, A. G., Dudenko, A. I. & Petrini, D. (2002). *J. Phys. B At. Mol. Opt. Phys.* **35**, 395–399.
Lowe, J. A., Chantler, C. T. & Grant, I. P. (2010). *Phys. Lett. A*, **374**, 4756–4760.
Lowe, J. A., Chantler, C. T. & Grant, I. P. (2011). *Phys. Rev. A At. Mol. Opt. Phys.* **83**, 060501.
Lu, C. C., Malik, F. B. & Carlson, T. A. (1971). *Nucl. Phys. A*, **175**, 289–299.
McCrary, J. H., Singman, L. V., Ziegler, L. H., Looney, L. D., Edmonds, C. M. & Harris, C. E. (1971). *Phys. Rev. A*, **4**, 1745–1750.
Melia, H. A., Dean, J. W., Smale, L. F., Illig, A. J. & Chantler, C. T. (2019). *X-ray Spectrom.* In the press.
Mendenhall, M. H., Henins, A., Hudson, L. T., Szabo, C. I., Windover, D. & Cline, J. P. (2017). *J. Phys. B At. Mol. Opt. Phys.* **50**, 115004.
Mukoyama, T. & Taniguchi, K. (1987). *Phys. Rev. A*, **36**, 693–698.
Nelson, G. C. & Saunders, B. G. (1969). *Phys. Rev.* **188**, 108–112.
Parratt, L. G. (1936*a*). *Phys. Rev.* **49**, 502–507.
Parratt, L. G. (1936*b*). *Phys. Rev.* **50**, 1–15.
Parratt, L. G. (1959). *Rev. Mod. Phys.* **31**, 616–645.
Pham, T. L., Nguyen, T. V. B., Lowe, J. A., Grant, I. P. & Chantler, C. T. (2016). *J. Phys. B At. Mol. Opt. Phys.* **49**, 035601.
Salem, S. & Wimmer, R. (1970). *Phys. Rev. A*, **2**, 1121–1123.
Sauder, W. C., Huddle, J. R., Wilson, J. D. & Lavilla, R. E. (1977). *Phys. Lett. A*, **63**, 313–315.
Scofield, J. (1974). *Phys. Rev. A*, **9**, 1041–1049.
Scofield, J. H. (1969). *Phys. Rev.* **179**, 9–16.
Smale, L. F., Chantler, C. T. & Kimpton, J. A. (2015). *X-ray Spectrom.* **44**, 54–62.
Sorum, H. (1987). *J. Phys. F Met. Phys.* **17**, 417–425.
Sorum, H. & Bremer, J. (1982). *J. Phys. F Met. Phys.* **12**, 2721–2728.
Sulentic, J. W., Marziani, P., Zwitter, T., Calvani, M. & Dultzin-Hacyan, D. (1998). *ApJ*, **501**, 54–68.
Uo, M., Wada, T. & Sugiyama, T. (2015). *Jpn. Dent. Sci. Rev.* **51**, 2–9.